Flow Measurement and Instrumentation 87 (2022) 102212

Contents lists available at ScienceDirect

Flow Measurement and Instrumentation

journal homepage: www.elsevier.com/locate/flowmeasinst

Measurement of turbulent supersonic steam jet flow characteristics using TDLAS

Ahmed Al-Manea [a,b,*], D. Buttsworth [a], K. Saleh [a], R. Malpress [a], John Leis [a]

[a] School of Mechanical and Electrical Engineering, University of Southern Queensland, Toowoomba, Queensland, 4350, Australia
[b] Al-Samawah Technical Institute, Al-Furat Al-Awsat Technical University, Al-Samawah, 66001, Iraq

ARTICLE INFO

Keywords:
Ejectors
Turbulent
Fluid mechanic
Multiphase flow
TDLAS

ABSTRACT

Ejectors have no moving parts and are preferable to mechanical compressors in many applications, but ejectors typically have a relatively low efficiency. To aid in the ejector design process, thorough understanding of the turbulent mixing of multi-phase compressible jets is beneficial.

This paper reports experimental results for Tunable Diode Laser Absorption Spectroscopy (TDLAS) measurements derived from an axisymmetric supersonic steam jet apparatus.

In this experimental work, a supersonic steam jet nozzle exit of a diameter 13.6 mm was surrounded by a low-speed flow of dry nitrogen. The TDLAS system was traversed through the flow at three different planes downstream from the ejector nozzle exit: 15, 20, and 30 mm distance. At each of the three planes, line-of-sight measurements were made with the laser passing through locations between 0 and 15 mm from the jet centreline.

Through the analysis of the TDLAS data and application of the Abel inversion method, the radial distribution of the pressure, temperature, and the concentration of the water-vapour were obtained. The key findings are that it is possible to determine key physical parameters using experimental TDLAS measurements when combined with a suitable numerical optimization approach.

1. Introduction

Ejectors have no moving parts and are preferable to mechanical compressors in thermal refrigeration systems which utilize low-grade heat sources. However, ejectors typically have a relatively low efficiency. Efforts to understand the dominant factors which control the mixing-induced entrainment of the low pressure stream inside ejectors are an on-going research topic. In the case of steam ejectors, additional complexity in the mixing process arises because the steam expansion in the supersonic nozzle typically causes condensation. The mixing between the high speed and low speed flows in a steam ejector involves the supersonic turbulent mixing of two-phase flow in the presence of pressure gradients. This provides substantial challenges for modelling and simulation.

In spite of the significant progress that has been achieved in this field, reliable steam ejector modelling remains a problem that has yet to be resolved. Due to the flow complexity resulting from simultaneous interaction of numerous factors that effect the mixing process of the primary and secondary streams, obtaining a reliable model of the mixing process remains a difficulty still to be overcome.

Few experimental studies on condensation in ejectors can be found in the literature. Fundamental experiments on condensation effects in steam nozzles have been performed [1,2]. In such works, measurements of static pressure distribution along steam nozzles are presented. Results from such studies have subsequently been used by many researchers for model validation [3]. Visualization techniques have also been used to study the jet structure and the mixing inside ejectors. A Schlieren technique was used in [4] to investigate the flow structure at the entry of the mixing chamber of an ejector. This study concluded that a wake was observed in the region of the shear layer downstream the nozzle exit, and this wake effects the mixing between the primary and secondary streams.

Schlieren methods have also been used to study the shock wave structure at the supersonic nozzle exit with the outcome that when the streamwise length of the shock wave pattern is reduced, an enhancement in ejector performance is also observed [5–7].

A shadowgraph technique was used in [8] to visualize the primary flow jet at different superheated levels using R134a. It was found that at a higher degree of condensation (lower superheated conditions), the ejector performance decreases

* Corresponding author at: Al-Samawah Technical Institute, Al-Furat Al-Awsat Technical University, Al-Samawah, 66001, Iraq.
E-mail address: Dr.ahmed.almanea@atu.edu.iq (A. Al-Manea).

https://doi.org/10.1016/j.flowmeasinst.2022.102212
Received 31 August 2021; Received in revised form 2 July 2022; Accepted 6 July 2022
Available online 11 July 2022

Particle Image Velocimetry (PIV) techniques have also been employed to obtain the velocity vector distribution to visualize the shock pattern within an ejector, and to characterize the mixing within the ejector [9,10].

Laser tomography techniques have been used to visualize the supersonic flows and provide details about the flow structure. The method reported in [11] uses laser light sheet, scattering tracers, and an optical arrangement.

The objective of previous studies of steam ejectors may be classified into two areas: (a) improving the matching of ejector performance to variable source/load characteristics for overall system efficiency gains [12–17]; (b) improving ejector performance at fixed operating points [18–21]. In order to achieve these objectives, three different approaches were used: one-dimensional modelling, physical experiments, and computational fluid dynamic (CFD) simulations [22–26].

Over the past decades, significant work has been performed in the area of Tunable Diode Laser Absorption Spectroscopy (TDLAS) techniques [27–30]. Measurements of the temperature and water mole fraction using this technique have been extensively studied and implemented for flame measurement [31–36].

An experimental study utilizing this technique was performed to study the lineshape measurements in combustion gases [37]. This technique was also used to measure atmospheric gas concentration for pollution studies [38]. Lasers have become a good-quality choice for flow analysis studies due to their narrow linewidth, high spectral intensity, simple and fast tuning of the wavelength and compactness [39]. The robustness and fast response of TDLAS sensors have led to rapid progress in application of these sensors to practical combustors, and TDLAS systems have the potential to be applied in control applications [40].

The TDLAS technique is suited to measurement of water-vapour temperature and concentration in combustion. [30] conducted experimental studies using the TDLAS method for the measurements of line-of-sight of water-vapour temperature in three different facilities: (1) pulse detonation engines; (2) gas turbine rig; and (3) a scramjet combustor. The authors used the integrated area ratio method and concluded that TDLAS can to be used to measure the species parameters over a wide range of conditions [32–36].

The TDLAS studies have shown that this technique can be used to measure the temperature, pressure, and the concentration of the target species in a wide variety of applications, but no studies using TDLAS for ejector flows have been reported. The limited amount of experimental data on condensation in two-stream compressible turbulent shear layers, combined with the inability of wet-steam models of fully simulate the flow in steam ejectors, indicates the need for further experimental investigations.

In the current study, TDLAS approaches were adopted and redesigned to formulate a new approach to investigate the mixing development between two streams. Measuring the radial distribution of the water-vapour concentration, the static pressure, and static temperature can contribute new knowledge in supersonic turbulent mixing development and provide experimental reference data for model development.

2. TDLAS theoretical background

The TDLAS technique is well established in the literature [27]. TDLAS relies on the reduction in optical power of a laser beam as it passes through a gas. This reduction can be used in conjunction with the HITRAN parameter database to infer the flow properties. HITRAN stands for high-resolution transmission molecular absorption; it is an online database comprising a combination of spectroscopic parameters which are used to simulate the transmission of light at different conditions and wavelengths [41].

Table 1
Geometry design dimensions of co-flow apparatus.

	Geometric parameters	Dimension in (mm)
1	Diameter of the secondary inlet	90
2	Nozzle Exit Position (NXP)	+15
3	Mixing chamber length	420
4	Mixing chamber diameter	90
5	Diffuser outlet diameter	94
6	Diffuser outlet diameter	94

Transmission of light at a particular wavelength, through a particular medium, can be described by the Beer–Lambert relation:

$$T = \frac{I_t}{I_o} = \exp(-k_v.L) \tag{1}$$

where I_o and I_t are the respective beams intensities before and after passing through the medium, k_v is the spectral absorbance coefficient (cm^{-1}), and L is the beam path length (cm). The value of k_v for an individual spectral line can be defined as [42]

$$k_v = S(T).\phi(v).N_d \tag{2}$$

where, $S(T)$ is the line strength at a certain wavenumber v (cm^{-1}/molecules cm^{-2}), $\phi(v)$ is the line shape function ($1/cm^{-1}$), N_d is the number of the absorbing molecules per unit volume, and can be calculated as

$$N_d = N_L.P_T.X_{abs}.\left(\frac{296}{T}\right) \tag{3}$$

where T is the temperature (K), P_T is the total pressure (atm). X_{abs} is the mole fraction of absorbing medium, and N_L is the Loschmidts' number, $N_L = 2.447 \times 10^{19}$ (mol cm^{-3} atm^{-1}) at 296 K.

3. Experimental arrangement

3.1. Supersonic steam jet apparatus

A photograph of the supersonic steam jet experimental apparatus is shown in Fig. 1. A schematic diagram is shown in Fig. 2. As can be seen it, is divided into two parts: the high pressure and temperature subsystem (shown in the right-hand box in Fig. 2), and the low pressure and temperature sub-system (shown in the left-hand box in Fig. 2).

The system was evacuated using a vacuum pump connected to the end of the condenser at location (6). When the condenser reached an absolute pressure between 1.5 and 2 kPa, the valve at (5) was opened to evacuate the test section from air. At (7) and (8), a cold water-recirculation system was used to provide the condenser unit with cold water flowing through the annular gap between the PVC tube and the brass tube. In order to condense the discharged steam during the test, cold water was maintained within a temperature range of 6–10 °C via heat exchange within the reservoir which contained ice for this purpose. Around 100 kg of ice was consumed during each experiment. Details on the mixing chamber of the apparatus is illustrated in Table 1.

In the high pressure sub-system, a steam generator was used to deliver steam at a high pressure and temperature into the primary nozzle. The steam was at saturation conditions but not superheated. The target operating condition for the primary superheated steam was 150 kPa and 113 °C, and this was achieved using a trace heating element with a power of 300 W and 1 m length, wrapped around the 12.5 mm copper tube. This was found to be sufficient to increase the temperature of the saturated steam by 5 °C. A pressure regulator was used to adjust the pressure delivered by the steam generator. The valve near (2), was used to drain the condensate from the boiler during heat-up. The superheated steam was fed into the test section by opening the valve near Section 3. The system reached stable primary nozzle conditions as specified in Table 2 after approximately 10 min.

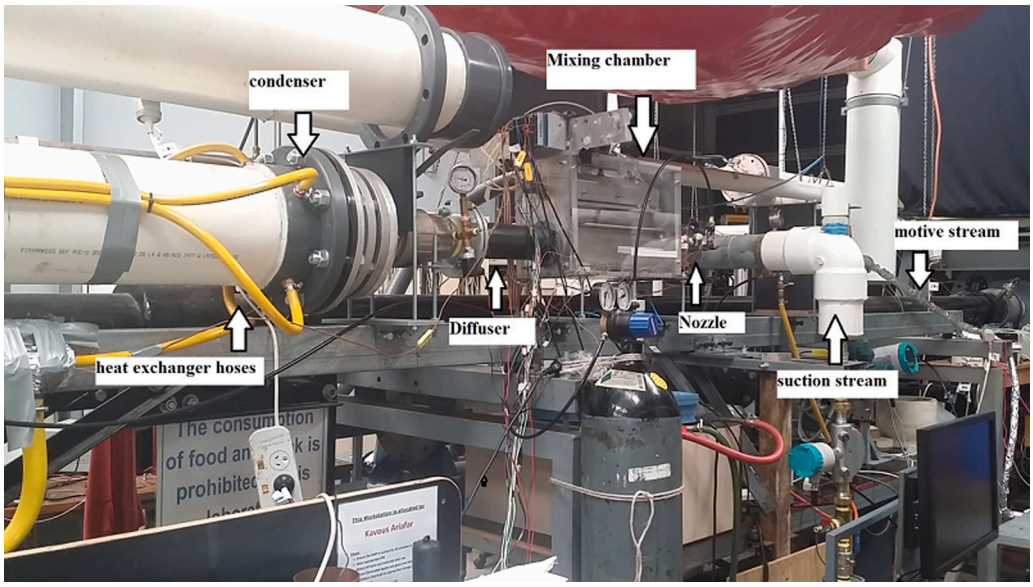

Fig. 1. Photograph of the supersonic steam jet apparatus.

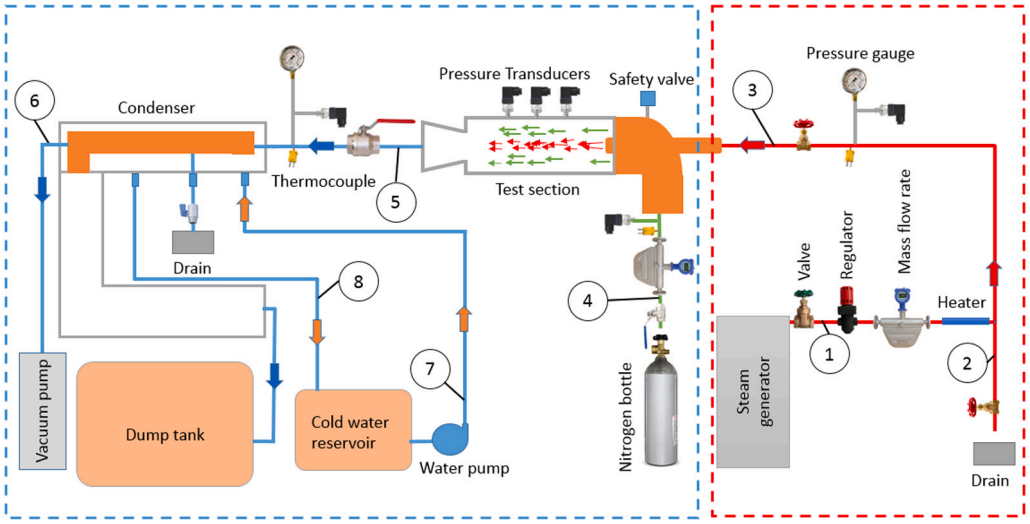

Fig. 2. Schematic diagram of the ejector facility setup.

Table 2
Operating conditions for the supersonic steam jet co-flow apparatus.

	Stream	Pressure (kPa)	Temperature (°C)	Mass flow (g/s)
1	Primary (steam)	150	120	1.8
2	Secondary (nitrogen)	3.4	34	5.5–6.5
3	Condenser	2–4	–	–

In this study, a convergent–divergent nozzle was used as the primary nozzle which delivered the high energy steam to the ejector. The area ratio A_T is estimated from standard ESDU86030 [43], and to be 17.4. To provide a non-absorbing co-flowing stream that enabled the supersonic wet steam jet absorption to dominate the TDLAS line-of-sight measurements, nitrogen was used in the apparatus as the secondary stream. An evacuated dump tank was connected to the end of the condenser in order to keep the pressure sufficiently low. Even with the additional dump tank volume, it was necessary for the secondary flow valve (4), to be opened for only 10 s for the purpose of taking measurements.

3.2. TDLAS hardware and measurement arrangements

The key components which were used in TDLAS arrangement are: (1) laser source, a tunable diode laser (EP1392-DM-DX1) which has the ability to generate a range of wavelengths by changing the bias current. This laser was designed specifically for water-vapour detection. The laser diode temperature and current was controlled so as to generate a beam with wavelength in the range between 1392 and 1393 nm at a frequency of 10 Hz; (2) a balanced photoreceiver (New Focus Model 2017 Nirvana) was also used to detect the laser beam, which has the advantage of reducing several noise sources that can compromise measurement accuracy. This approach was able to minimize common-mode noise and more effectively amplify the absorption signals of interest; (3) the laser traversing mechanism, which has been designed to control the laser movement in vertical and horizontal directions within the supersonic jet facility; (4) additional hardware such as function generators, oscilloscopes, beam-splitter, attenuator and the laser driver were also used during the experiments. Table 3 shows the specifications of scientific instruments and associated apparatus used for the TDLAS measurements. The cm^{-1}, unit is used in the HITRAN

Table 3
Specifications of TDLAS components (Source: ThorLabs).

	Components	Specifications
1	Tunable Diode Laser	range between 1392 and 1393 nm
2	Balanced photoreceiver	Nirvana2017, wavelength 800–1700 nm
3	Laser voltage control box	bias voltage range 0–1.2 V
4	Fibre couplers	ThorLabs TW1300R3A1
5	Attenuator	ThorLabs VOA50-APC, wavelengths 1310 ± 20 /1550 ± 20 nm
6	laser collimator	ThorLabs C230TMD-C, wavelengths 1050–1700 nm

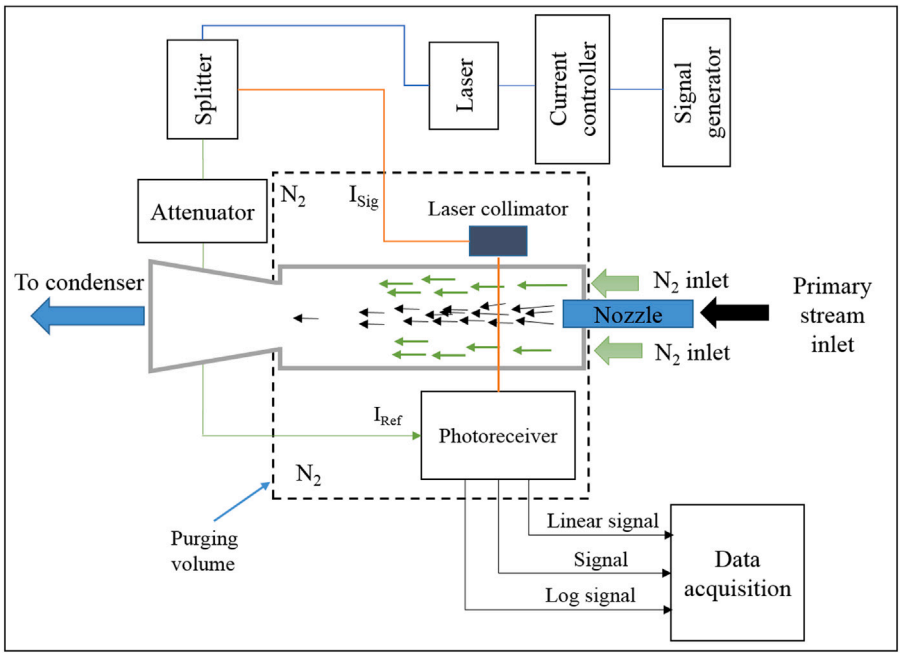

Fig. 3. Schematic diagram of the test section and TDLAS system arrangement.

database, however the laser wavelengths are specified in nm. For a given wavelength of ν cm^{-1}, the corresponding wavelength is $\lambda = \frac{10^7}{\nu}$ nm.

4. Experimental measurements

Fig. 3 shows a schematic diagram of the experimental arrangement which was used to study the supersonic jet development. The laser was positioned opposite the balanced photoreceiver, so that the laser beam was normal to the flow direction. The laser beam was collimated at the cylinder's centreline before it passed through the test section. The transmitted laser beam was initially detected from the exit side of the test section by using a luminescent card. The laser beam position was aligned precisely to fall on the signal input of the balanced photoreceiver unit.

When an adequate signal was received by the balanced photoreceiver (SNR ≥ 5 dB), the split ratio was adjusted between the signal beam and the reference beam to approximately 2.

The movement mechanism was designed to move the laser-detector unit in both downstream and radial directions. The TDLAS measurements were made for three locations downstream of the nozzle exit at 15 mm, 20 mm, and 30 mm. At each downstream station, the measurements were recorded for the laser between 0 and 15 mm from the nozzle centreline in increments of 1 ±0.1 mm. At each radial location the split ratio of the balanced photoreceiver was adjusted to remain as close to 2 as possible. The secondary stream valve was opened for around 10 s, with the TDLAS measurements were recorded approximately 2 s after the flow commenced in order to stabilize the conditions. Subsequently, the experimental data was acquired for around 8 seconds.

5. Signal post-processing

The post-processing for the collected signal at all of the three locations downstream from the primary nozzle included the following: (1) obtaining the mean absorption spectrum from approximately 80 scans; (2) applying Voigt fitting to smooth the data; (3) applying the Abel inversion algorithm to reconstruct the radial distribution of absorption coefficient from the smoothed absorbance data; (4) identifying the three unknown parameters: the pressure, temperature, and concentration using least-squares error assessment of the absorption coefficient against the HITRAN database.

5.1. Voigt fitting

Approximately 80 scans at each station were averaged in order to reduce the effects of noise. A Voigt fit was applied to facilitate comparison with the simulated theoretical profile. The Voigt fitting employed was based on the method of [44,45]. A MATLAB® script was developed to implement the Voigt lineshape fitting algorithm, based upon the peak maximum absorbance magnitude, peak central wavenumber, Gaussian width, and Lorentzian width. Fig. 4 shows an example of Voigt fitting and the residual for data from an experiment at 15 mm downstream, and $y = 1$ mm. More details on the use of Voigt fitting are given in a previous study [46].

5.2. Abel inversion algorithm

Since the objective of this study is to recover the radial distribution of the jet water-vapour concentration, $F(r)$, the symmetric Abel transform is an appropriate theoretical construct. Fig. 5 illustrates

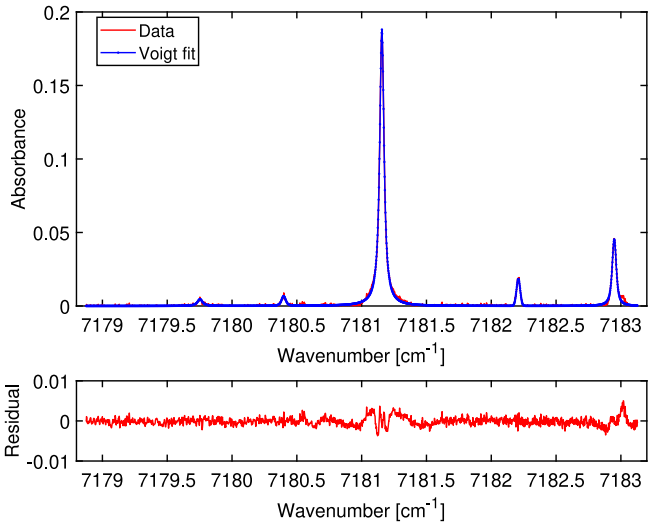

Fig. 4. Illustration of Voigt fit and residual for data obtained at 15 mm downstream the nozzle, $y = 1$ mm.

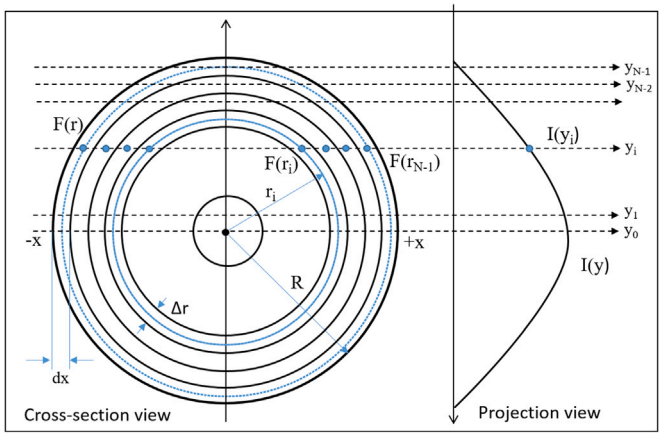

Fig. 5. Field discretization for the Abel inversion algorithm.

the nomenclature associated with the Abel inversion. The collected data represents a line-of-sight integrated effect, termed the projection data. The relationship between the projection data $I(y)$ and the radial distribution $F(r)$, can be described with Abel's equation [47]:

$$I(y) = 2\int_{y}^{R} \frac{F(r)\, r}{\sqrt{r^2 - y^2}}\, dr \tag{4}$$

Different approaches have been developed in the literature [47] to reconstruct the $F(r_i)$ distribution. In this study, the Three-Point-Deconvolution (TPD) method has been adopted, as it has a low noise relative to other methods [47]. The Abel inversion equation can be written as:

$$F(r) = -\frac{1}{\pi}\int_{r}^{R} \frac{I'(y)}{\sqrt{y^2 - r^2}}\, dy \tag{5}$$

The effect of noise in experimental data on the Abel inversion has been assessed with an example of a synthetic data in the previous work [46,48]. The post-processing is summarized in Fig. 6.

5.3. Fitting with simulated theoretical spectrum profiles

The first step is identifying concentration, pressure and temperature which minimizes the error between the coefficient of absorbance

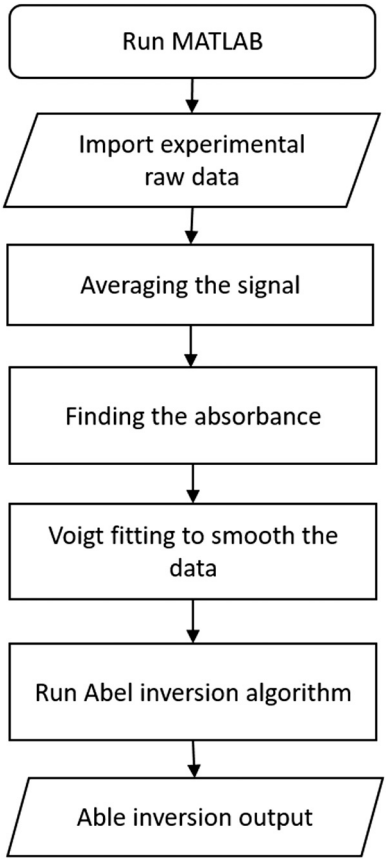

Fig. 6. Initial processing steps performed on experimental data.

k_v data and the results from the HITRAN database over a specified range of wavenumbers. This fitting is achieved by using the Levenberg–Marquardt optimization approach between the experimental absorbance coefficient k_v and the simulated theoretical spectra profile. The theoretical spectral profile was estimated using MATLAB script with aid of the HITRAN 2012 database [41] as follows:

1. Load HITRAN database to provide the algorithm with the necessary spectroscopic parameters for the transition lines with the wavenumber range between 7179 and 7183 cm^{-1}.
2. Establish an array of pressure, temperature, and concentration over which simulated absorption profiles are generated.
3. Use the MATLAB script to generate absorbance coefficient profiles at different conditions specified in step 2. This has been achieved by using Gaussian and Lorentzian lineshape functions. The Voigt profile also calculated for each condition using the spectroscopic equations.
4. Load the experimental data, starting from the Voigt fitting stage.
5. Apply a least-squares error method between the calculated theoretical absorbance coefficient profile and the experimental data for each pressure, temperature and mole fraction combination.

Fig. 7 summarizes these steps in a schematic diagram as applied to the experimental data.

6. Analysis method and assessment

The uncertainties in the TDLAS-derived parameters have been assessed using a similar method to that used in previous work [46], with some minor differences.

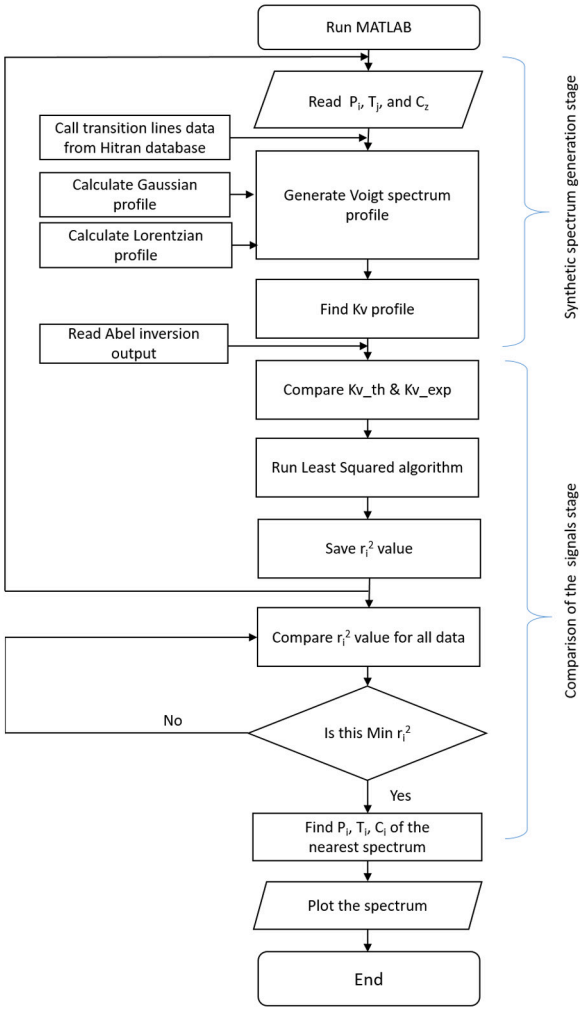

Fig. 7. Analysis steps for parameter estimation.

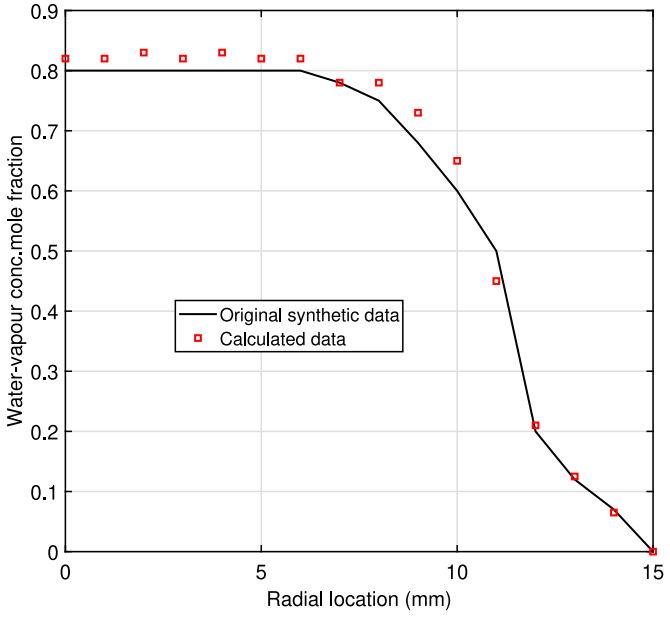

Fig. 8. Illustration of the synthetic concentration and the profile obtained from Abel inversion method.

A comparison of the synthetic concentration data and the reconstruction of that data using the method outlined above is shown in Fig. 8.

The differences between the synthetic data and the reconstructed results for the concentration, static pressure, and static temperature are used to define the uncertainties in the actual experimental profiles in each case. The differences between the specified concentration profile and the Abel inversion results ranged from 0%–10%. In the case of the static pressures, differences ranged from 0%–9%, and for the static temperatures, differences ranged from 0–5 K which in relative terms is between 0–1.7%.

7. Results and discussion

7.1. Absorbance profile

Figs. 9–11 shows the raw data after Voigt fitting step for the absorbance profile results at the three nominated downstream locations.

Fig. 9 shows the absorbance profile results for all the laser traverse locations at 15 mm downstream the nozzle. The absorbance results at this location show that the jet was narrow and contained a higher concentration of water-vapour near the jet centreline. It is also observed that there was no absorbance at laser traverse locations for $y > 7$ mm at the $x = 15$ mm position, because the water-vapour jet is narrow at this stage, since the primary nozzle exit diameter is 13.6 mm. The majority of the co-flow within this region is nitrogen.

Fig. 10 shows the absorbance profile results for all the laser traverse locations at 20 mm downstream the nozzle. At this position, the laser traverse locations from the jet axis up to 13 mm from the jet centreline were used.

Fig. 11 shows the absorbance profiles at a location 30 mm from the primary nozzle exit plane. The laser traverse measurements were taken between the jet centreline and 14 mm above the centreline.

7.2. Concentration profile

Fig. 12 shows the results of the reconstructed mole fraction of water-vapour at the three stations 15, 20, and 30 mm from the nozzle exit. The conditions of the flow at nozzle exit position are unstable due to the condensation phenomena of the steam at the nozzle throat. Thus, high water vapour concentration are expected along the centreline. Fig. 12 shows that at 15 mm downstream, the flow is characterized by higher concentration at the centreline of the jet, with a value around 93%, gradually decreasing to the radial of 7 mm. The expected value for the water-vapour mole fraction within the jet core flow is 100%, however, some deviation from this value may have arisen because: (1) error in the Abel inversion algorithm which was calculated to be around 6% near the centreline [46]; (2) the refraction of the laser beam from the droplets which exist in the laser path length.

However, measurements at station 20 mm have shown a rapid decrease of the radial mole fraction of the water-vapour that occurred from 75% at the jet centreline to zero at a radial location of 14 mm.

7.3. Static pressure profile

The radial static pressure at the three locations 15, 20, and 30 mm was also calculated as shown in Fig. 13. At the 15 mm position, the jet pressure has a slightly higher value than the co-flow pressure and a peak is registered at the radial location 2 mm from jet centreline. Nonuniformities in static pressure within the jet can arise because of the supersonic wave structure that is established when the jet static pressure and flow direction do not match the co-flowing localized environment. At 20 mm, the laser beam within the region appears to have traversed shock and expansion waves because the pressure ranged in magnitude between 2.6 and 4 kPa, which is a larger range of values than encountered at 15 mm (Fig. 13). The radial profile of the static

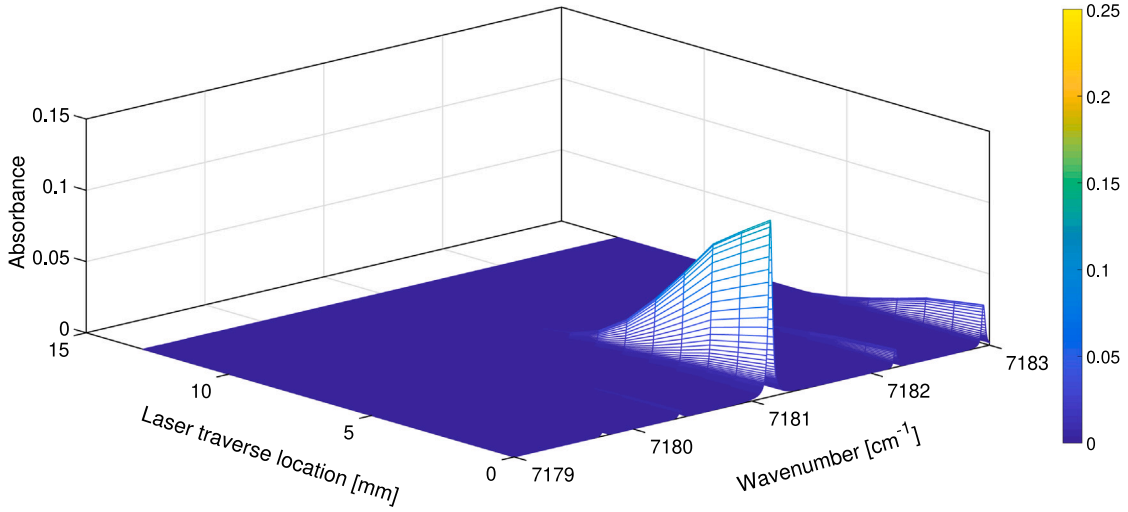

Fig. 9. Absorbance results at 15 mm downstream of the nozzle exit.

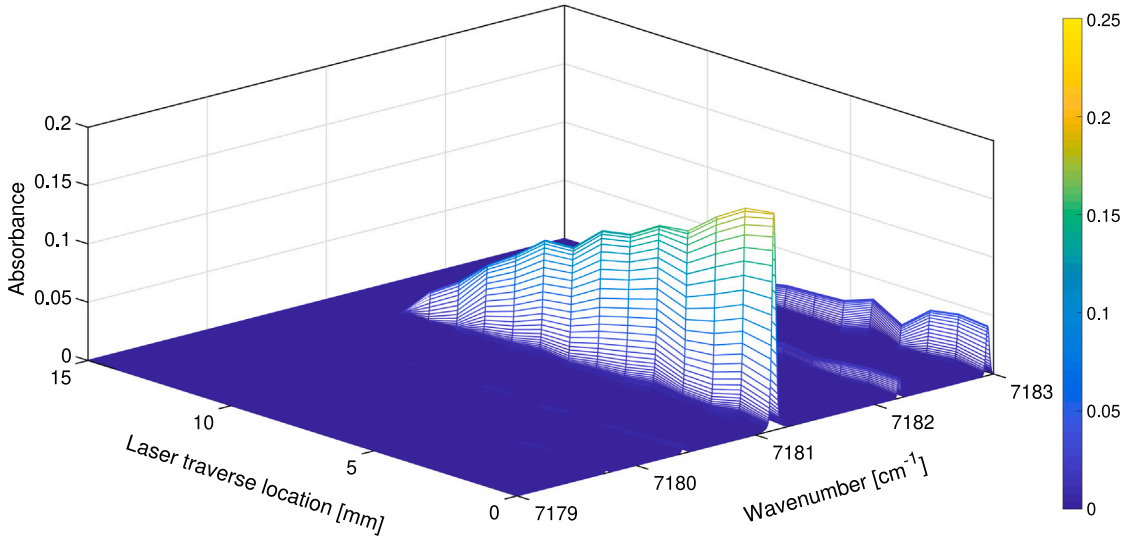

Fig. 10. Absorbance results at 20 mm downstream of the nozzle exit.

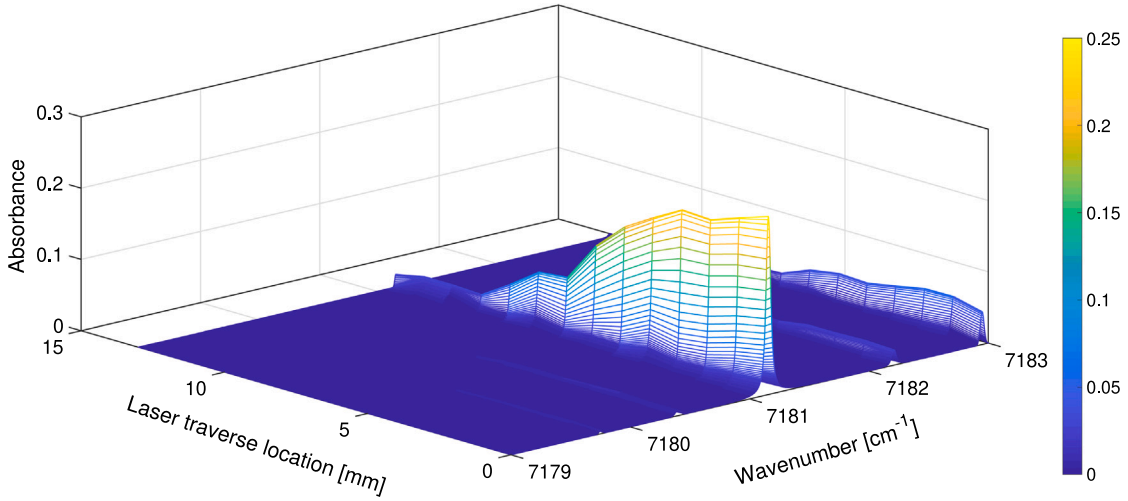

Fig. 11. Absorbance results at 30 mm downstream of the nozzle exit.

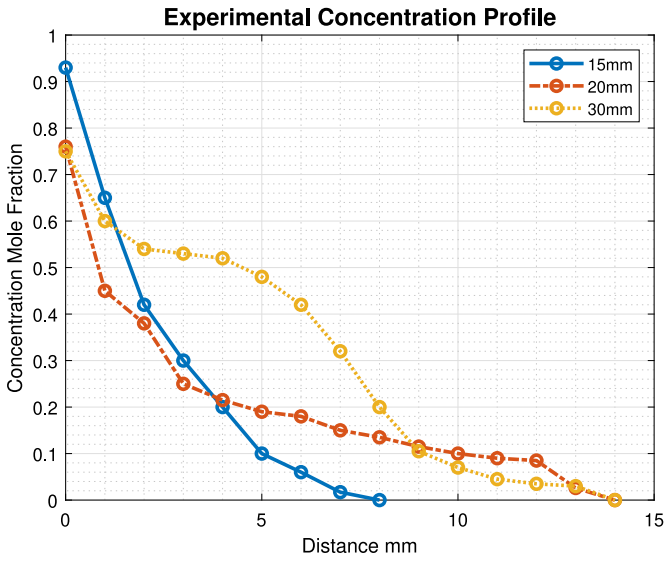

Fig. 12. Water vapour mole fraction profile at various downstream measurement lines.

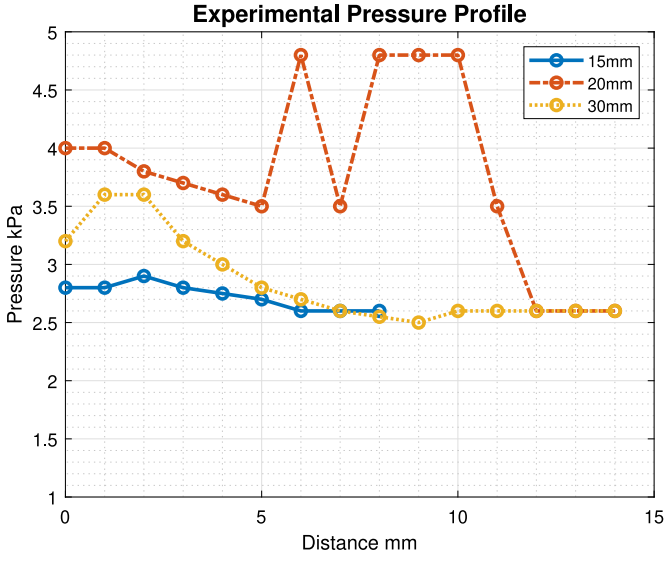

Fig. 13. Static pressure profile at various downstream measurement lines.

pressure at 30 mm shows elevated pressure close to the axis of the jet, followed by a decrease in pressure with increasing distance after a radial location 3 mm from the jet axis. At this point, the flow static pressure reaches the shear layer region.

7.4. Static temperature profile

Fig. 14 illustrates the radial static temperature profile at the three downstream locations 15, 20, and 30 mm. At 15 mm, the static temperature increased from 290 K at the jet centreline to 330 K at a radial location of 7 mm from the jet centreline.

However, at 20 mm, the static pressure near the jet centreline is higher than at 15 mm, as is the static temperature, which is consistent with a compression process occurring near the centreline between 15 mm and 20 mm. A sharp peak in temperature increase was noted at a radial location of 6 mm from the jet centreline, and this also appears consistent with the pressure results in which elevated pressures are observed in this vicinity.

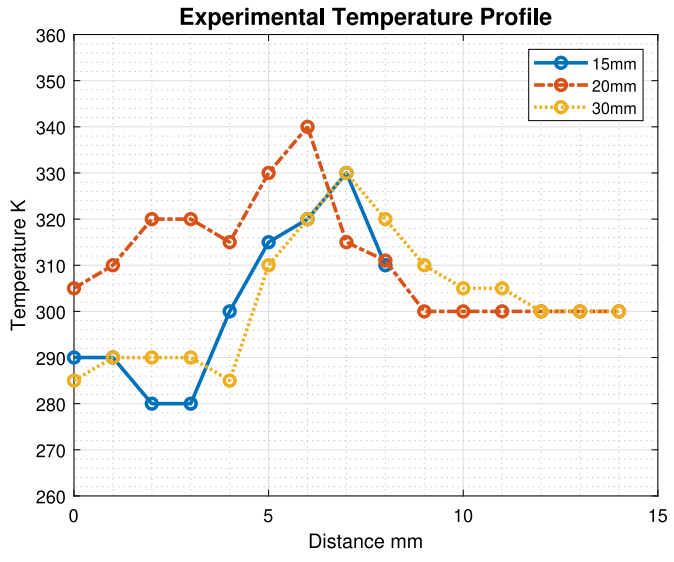

Fig. 14. Temperature profile at various downstream measurement lines.

The radial static temperature at 30 mm varied between 285 and 300 K in radial locations between 0 and 14 mm from the jet centreline. The maximum temperature was 330 K at the radial location of 7 mm. The presence of a peak in the temperature profile at a location where the static pressure profile is varying monotonically suggests an energy exchange which is decoupled from the flow pressure. Such exchange may be associated with mixing in the free shear layer. At lower radial locations, the water-vapour temperature decreases towards that of the co-flowing nitrogen at around 300 K.

8. Conclusion

In this study, an apparatus was established to study the mixing between a supersonic steam jet and a co-flowing stream of nitrogen. The apparatus was designed to accommodate the adopted TDLAS measurement technique and to probe a supersonic co-flow system. The inverse Abel transformation was used to determine the spatial properties of the jet flow development at the three nominated locations. Three locations downstream of the primary supersonic nozzle were chosen to study the flow structure: 15, 20, and 30 mm, and the reconstructed water-vapour concentration, static pressure and static temperature were determined. Due to the condensation phenomena, the highest value of water-vapour concentration was measured at 15 mm from the primary nozzle. The radial static pressure measurements show signs of shock and expansion waves at 20 mm, with magnitudes ranging between 2.6 and 4 kPa compared with the other positions. Observation of the radial temperature values at 20 mm are consistent with the compression process near the centreline between 15 mm and 20 mm. TDLAS measurements have shown the ability to reveal flow characteristics in terms of the supersonic jet's shock wave and shear layer structure. The findings are consistent with previous studies [17] in terms of fluctuations in the flow conditions. Uncertainties were calculated in the actual experimental profiles in each case; for the static pressures, differences ranged from 0%–9%, and for the static temperatures, differences ranged from 0 – 5 K, which in relative terms is between 0 – 1.7%. This work's key contribution is applying the tomographic approach to enhance the understanding of the radial distribution of wet-steam supersonic jet flows.

9. Recommendations for future work

For future work, the following can be investigated:

- The measurement of the wet-steam jet characteristics could be further investigated using a Wavelength-Modulation Spectroscopy (WMS) method. In this method, the temperature along the jet core could be extracted from the ratio of the first and second harmonic signals.
- Improvements to the TDLAS method could be achieved if using a suitable tunable laser which could be modulated at a high frequency. The present work was limited to frequency around 10 Hz; future work should target modulation at around 1 kHz or more.
- Further improvement in the development of a non-equilibrium wet-steam CFD model to simulate the mixing between the steam and the nitrogen. This can be done by adding a user-defined-function to extend the current limitation of the wet-steam model in the ANSYS FLUENT 18.1 CFD simulations.

Declaration of competing interest

The authors declare that they have no known competing financial interests or personal relationships that could have appeared to influence the work reported in this paper.

Data availability

Data will be made available on request.

References

[1] M. Moore, P. Walters, R. Crane, B. Davidson, Predicting the fog-drop size in wet-steam turbines, Heat Fluid Flow Steam Gas Turbine Plant 4 (1973) 101–109.

[2] C.A. Moses, G.D. Stein, On the growth of steam droplets formed in a laval nozzle using both static pressure and light scattering measurements, J. Fluids Eng. 100 (3) (1978) 311–322.

[3] L. Zori, F. Kelecy, Wet steam flow modeling in a general CFD flow solver, in: 35th AIAA Fluid Dynamics Conference and Exhibit, Toronto, Canada, 2005.

[4] V. Dvorak, P. Safarik, Supersonic flow structure in the entrance part of a mixing chamber of 2D model ejector, J. Therm. Stresses 12 (4) (2003) 344–349.

[5] Y. Zhu, P. Jiang, Experimental and numerical investigation of the effect of shock wave characteristics on the ejector performance, Int. J. Refrig. 40 (2014) 31–42.

[6] P. Desevaux, A. Bouhanguel, L. Girardot, E. Gavignet, On the use of laser tomography techniques for validating cfd simulations of the flow in supersonic ejectors, Int. J. Fluid Mech. Res. 40 (1) (2013).

[7] Z. Chen, C. Dang, E. Hihara, Investigations on driving flow expansion characteristics inside ejectors, Int. J. Heat Mass Transfer 108 (2017) 490–500.

[8] A.B. Little, S. Garimella, Shadowgraph visualization of condensing R134a flow through ejectors, Int. J. Refrig. 68 (2016) 118–129.

[9] J. Gagan, K. Smierciew, D. Butrymowicz, J. Karwacki, Comparative study of turbulence models in application to gas ejectors, Int. J. Therm. Sci. 78 (2014) 9–15.

[10] A. Bouhanguel, P. Desevaux, E. Gavignet, Flow visualization in supersonic ejectors using laser tomography techniques, Int. J. Refrig. 34 (7) (2011) 1633–1640.

[11] P. Desevaux, O. Aeschbacher, Numerical and experimental flow visualizations of the mixing process inside an induced air ejector, Int. J. Turbo Jet Eng. 19 (1–2) (2002) 71–78.

[12] Y. Allouche, C. Bouden, S. Varga, A CFD analysis of the flow structure inside a steam ejector to identify the suitable experimental operating conditions for a solar-driven refrigeration system, Int. J. Refrig. 39 (2014) 186–195.

[13] M. El Hassan, A. Gubanov, W. May, R. Martinuzzi, Numerical investigation of the flow dynamics of a supersonic fluid ejector, in: Proceedings of the International Conference on Heat Transfer and Fluid Flow, Prague, Czech Republic, 2014, 171–1–7.

[14] K. Aldas, F. Şen, I. Ozkul, The investigation of gas ejector performance using CFD modelling, TEM 2 (2) (2013).

[15] R.K. McGovern, K.V. Bulusu, M.A. Antar, J.H. Lienhard, One-dimensional model of an optimal ejector and parametric study of ejector efficiency, in: 25th International Conference on Efficiency, Cost, Optimization and Simulation of Energy Conversion Systems and Processes, ECOS 2012, Perugia, Italy, 2012.

[16] T. Aravind, P.R. Reddy, S. Baserkoed, Thermal analysis of steam ejector using CFD, Int. J. Innov. Res. Sci., Eng. Technol. 3 (2014) 18311–18318.

[17] G. Al-Doori, D.R. Buttsworth, Pitot pressure measurements in a supersonic steam jet, Exp. Therm Fluid Sci. 58 (2014) 56–61.

[18] Y.-J. Chang, Y.-M. Chen, Enhancement of a steam-jet refrigerator using a novel application of the petal nozzle, Exp. Therm Fluid Sci. 22 (3–4) (2000) 203–211.

[19] S.M. Rao, G. Jagadeesh, Novel supersonic nozzles for mixing enhancement in supersonic ejectors, Appl. Therm. Eng. 71 (1) (2014) 62–71.

[20] N. Ruangtrakoon, S. Aphornratana, T. Sriveerakul, Experimental studies of a steam jet refrigeration cycle: Effect of the primary nozzle geometries to system performance, Exp. Therm Fluid Sci. 35 (4) (2011) 676–683.

[21] A. Al-Manea, T. Al-Jadir, Effect of ejector design parameters on flow structure inside the mixing chamber, IOP Conf. Ser.: Earth Environ. Sci. 779 (1) (2021) 012033.

[22] S. Varga, A.C. Oliveira, B. Diaconu, Numerical assessment of steam ejector efficiencies using CFD, Int. J. Refrig. 32 (6) (2009) 1203–1211.

[23] X. Wang, J. Dong, A. Li, H. Lei, J. Tu, Numerical study of primary steam superheating effects on steam ejector flow and its pumping performance, Energy 78 (2014) 205–211.

[24] F. Mazzelli, A.B. Little, S. Garimella, Y. Bartosiewicz, Computational and experimental analysis of supersonic air ejector: turbulence modeling and assessment of 3D effects, Int. J. Heat Fluid Flow 56 (2015) 305–316.

[25] F. Mazzelli, D. Brezgin, I. Murmanskii, N. Zhelonkin, A. Milazzo, Condensation in supersonic steam ejectors: Comparison of theoretical and numerical models, in: International Conference on Multiphase Flow, ICMF, May 22nd – 27th, Firenze, Italy, 2016.

[26] A. Al-Manea, K. Saleh, Supersonic steam ejectors: Comparison of dry and wet-steam CFD simulation models, J. Eng. Sci. Technol. 17 (2) (2022) 1200–1212.

[27] X. Zhou, Diode Laser Absorption Sensors for Combustion Control (Ph.D. thesis), Stanford University, 2005.

[28] A. Guha, I. Schoegl, Tomographic laser absorption spectroscopy using Tikhonov regularization, Appl. Opt. 53 (34) (2014) 8095–8103.

[29] R.K. Hanson, J.B. Jeffries, M.G. Allen, Tunable diode laser absorption sensor applications to aeropropulsion testing, in: Applied Vehicle Technology Panel Specialists' Meeting on Recent Developments in Non-Intrusive Measurement Technology NATO RSM-017, American Institute of Aeronautics and Astronautics, Citeseer, Budapest, Hungary, 2005.

[30] R. Hanson, J. Jeffries, Diode laser sensors for ground testing, in: 25th AIAA Aerodynamic Measurement Technology and Ground Testing Conference, San Francisco, California, 2006, p. 3441.

[31] A. Griffiths, A. Houwing, Measurements of temperature and water vapour concentration in a scramjet combustor, Measurements 13 (2004) 17.

[32] M. Arroyo, S. Langlois, R. Hanson, Diode-laser absorption technique for simultaneous measurements of multiple gasdynamic parameters in high-speed flows containing water vapor, Appl. Opt. 33 (15) (1994) 3296–3307.

[33] V. Nagali, R.K. Hanson, Design of a diode-laser sensor to monitor water vapor in high-pressure combustion gases, Appl. Opt. 36 (36) (1997) 9518–9527.

[34] X. Zhou, X. Liu, J.B. Jeffries, R. Hanson, Development of a sensor for temperature and water concentration in combustion gases using a single tunable diode laser, Meas. Sci. Technol. 14 (8) (2003) 1459.

[35] T. Cai, H. Jia, G. Wang, W. Chen, X. Gao, A sensor for measurements of temperature and water concentration using a single tunable diode laser near 1.4 μm, Sensors Actuators A 152 (1) (2009) 5–12.

[36] S. Li, A. Farooq, R.K. Hanson, H_2O temperature sensor for low-pressure flames using tunable diode laser absorption near 2.9 μm, Meas. Sci. Technol. 22 (12) (2011) 125301.

[37] R. Hanson, P. Kuntz, C. Kruger, High-resolution spectroscopy of combustion gases using a tunable IR diode laser, Appl. Opt. 16 (8) (1977) 2045–2048.

[38] J. Reid, J. Shewchun, B. Garside, E. Ballik, High sensitivity pollution detection employing tunable diode lasers, Appl. Opt. 17 (2) (1978) 300–307.

[39] M. Bolshov, Y.A. Kuritsyn, Y.V. Romanovskii, Tunable diode laser spectroscopy as a technique for combustion diagnostics, Spectrochem. Acta Part B: At. Spectrosc. 106 (2015) 45–66.

[40] S. Kim, J. Jeffries, R. Hanson, G. Raiche, Measurements of gas temperature in the arc-heater of a large scale arcjet facility using tunable diode laser absorption, in: 43rd AIAA Aerospace Sciences Meeting and Exhibit, Reno, Nevada, 2005, p. 900.

[41] L.S. Rothman, et al., The HITRAN2012 molecular spectroscopic database, J. Quant. Spectrosc. Radiat. Transfer 130 (2013) 4–50.

[42] Y. Yun, X. Zhao, Calculation of infrared absorption coefficients of dissolved gases in transformer oil, in: Electrical and Control Engineering (ICECE), 2010 International Conference on, IEEE, 2010, pp. 3431–3434.

[43] ESDU86030, Ejectors and jet pumps. Design for steam driven flow, Eng. Sci. Data Unit (1986).

[44] S. Abrarov, B.M. Quine, Efficient algorithmic implementation of the Voigt/complex error function based on exponential series approximation, Appl. Math. Comput. 218 (5) (2011) 1894–1902.

[45] R. Wells, Rapid approximation to the Voigt/Faddeeva function and its derivatives, J. Quant. Spectrosc. Radiat. Transfer 62 (1) (1999) 29–48.

[46] A. Al-Manea, D. Buttsworth, J. Leis, R. Choudhury, K. Saleh, Measurement of water vapour in axisymmetric jet development using TDLAS, in: Proceedings of the 21st Australasian Fluid Mechanics Conference, AFMC 2018, Adelaide, Australia, https://www.scopus.com/inward/record.uri?eid=2-s2.0-85084096675&partnerID=40&md5=871e73cc7ea756f840c04f214e46068e, Final, Cited by: 3.

[47] C.J. Dasch, One-dimensional tomography: A comparison of abel, onion-peeling, and filtered backprojection methods, Appl. Opt. 31 (8) (1992) 1146–1152.

[48] A. Al-Manea, D. Buttsworth, J. Leis, K. Saleh, Tunable diode laser absorption spectroscopy in a supersonic steam jet, in: IX Australian Conference on Laser Diagnostics, 2-4 Dec 2019, IX Australian Conference on Laser Diagnostics, Adelaide, Australia.